International Journal of Applied Earth Observation and Geoinformation 146 (2026) 104968

Contents lists available at ScienceDirect

International Journal of Applied Earth Observation and Geoinformation

journal homepage: www.elsevier.com/locate/jag

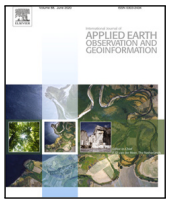

InSAR and GAT-LSTM integration for dam displacement prediction: Lessons from the Oldman River Dam, Canada

Ramin Farhadiani [a,*], Sayyed Mohammad Javad Mirzadeh [a], Ehsan Roshani [b], Daniel Cusson [b], Saeid Homayouni [a]

[a] Centre Eau Terre Environnement, Institut National de la Recherche Scientifique, Québec, QC, Canada
[b] National Research Council Canada, Ottawa, ON, Canada

ARTICLE INFO

Keywords:
Dam displacement
Oldman River Dam
InSAR
Forecasting
GAT-LSTM

ABSTRACT

The precise prediction of dam deformation is essential for ensuring infrastructure safety and mitigating geohazards, particularly in regions characterized by limited monitoring studies. This research concentrates on the Oldman River Dam in Alberta, Canada, where Interferometric Synthetic Aperture Radar (InSAR)-based deformation monitoring and prediction remain inadequately explored. A novel framework that integrates a Graph Attention Network with Long Short-Term Memory (GAT-LSTM) has been developed to address the limitations of existing methods, which neglect spatial dependencies among InSAR-derived points and the increased model complexity stemming from point clustering or InSAR time series decomposition. Sentinel-1 data from three passes were processed utilizing a full-resolution InSAR technique, resulting in semi-vertical deformation velocities that demonstrated consistent subsidence along the dam crest, with rates fluctuating from 5.08 to 6.23 mm/yr. A robust correlation between deformation and reservoir water levels was noted, with accelerated crest deformation during the 2017–2019 drawdown period and a potential risk identified due to a significant decline in water levels projected for 2023–2024. The GAT-LSTM model, which captures both spatial and temporal dynamics, outperformed the standard LSTM, achieving 83.64% accurate points compared to 76.90% for the LSTM in short-term forecasting, exhibiting notable reliability along the crest. The peak performance was observed on September 9, 2021, with a Root Mean Square Error of 0.30 ± 0.013 mm and a Mean Absolute Error of 0.22 ± 0.012 mm. The proposed framework would enhance dam safety monitoring by providing actionable short-term predictions, demonstrating potential transferability to other slow-moving infrastructure.

1. Introduction

The dam safety is consistently threatened by various drivers, i.e., overtopping caused by subsidence, excess reservoir capacity, internal erosion (piping), improper operational procedures and asset management, and external drivers such as earthquakes and landslides (Zhang et al., 2016; Zhou et al., 2024, 2025). These risks might lead to the dam failure, and consequently, extensive fatalities, ecological devastation, and financial and human crisis. The failure of Sardoba Reservoir in Uzbekistan on May 1, 2020 (Xiao et al., 2022; Xie et al., 2022b), is a tragic example, resulting in numerous deaths and significant environmental damage, underscoring the necessity for accurate dam safety monitoring and highlighting an urgent need to establish early warning systems.

Satellite-based Interferometric Synthetic Aperture Radar (InSAR) is now widely recognized as a viable alternative that provides accurate and extensive deformation data, capable of identifying even minute ground displacements (Hu et al., 2017; Yan et al., 2024). Xiao et al. (2022) investigated the Sardoba Dam failure in Uzbekistan using InSAR time series with Sentinel-1 data from 2017 to 2020 and detected differential settlement of about 60 mm at the failure section, with a maximum settlement of around 270 mm noted on the northern bank since the impoundment of the reservoir. These observed deformations, particularly near the failure zone, suggested that internal erosion was a likely cause of the breach. Sharifi and Hendry (2023) used the Sentinel-1 InSAR time series from 2015 to 2021 to monitor Oldman River Dam (ORD) in Canada and showed that the spillway and the slope of embankment had average deformation of 1.3 and 8.3 mm/yr, respectively. Transitioning to concrete gravity dams, Tavakkoliestahbanati et al. (2024) examined the Kakhovka Dam in Ukraine before

* Corresponding author.
E-mail addresses: ramin.farhadiani@inrs.ca (R. Farhadiani), sayyed-mohammad-javad.mirzadeh@inrs.ca (S.M.J. Mirzadeh), ehsan.roshani@nrc-cnrc.gc.ca (E. Roshani), Daniel.Cusson@nrc-cnrc.gc.ca (D. Cusson), saeid.homayouni@inrs.ca (S. Homayouni).

https://doi.org/10.1016/j.jag.2025.104968
Received 26 June 2025; Received in revised form 7 November 2025; Accepted 12 November 2025

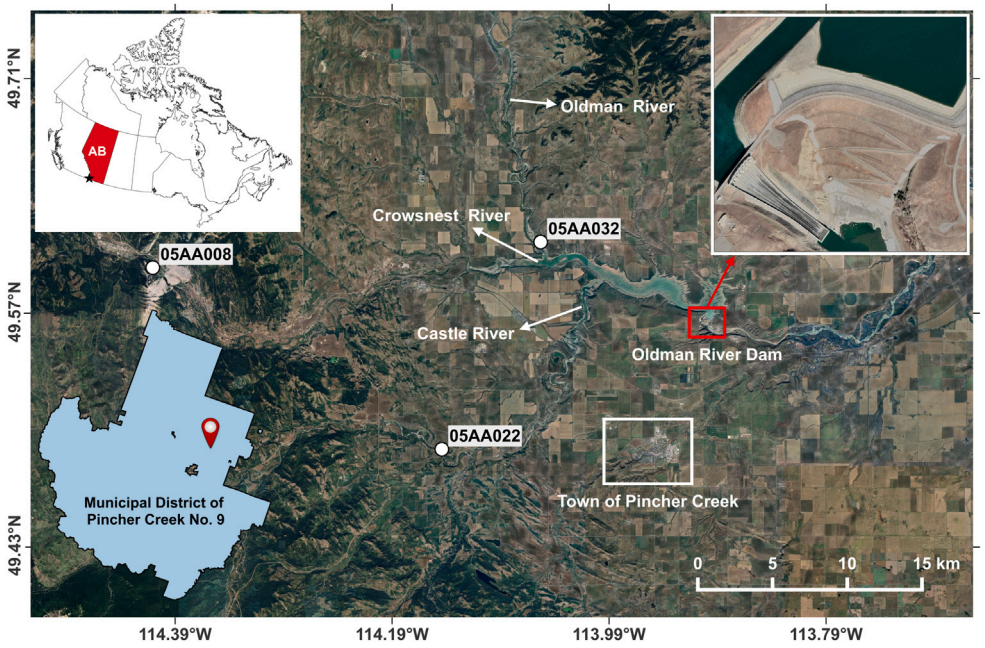

Fig. 1. The location of the Oldman River Dam, fed by the Crowsnest River, Castle River, and Oldman River, along with the surrounding hydrometric stations (05AA008, 05AA032, and 05AA022). Background image © Google Earth.

its collapse in 2023, using the Sentinel-1 data from 2017 to 2023, and observed an acceleration in the displacement in the concrete dam in June 2021 with a maximum rate of 22.7 mm/yr. Xie et al. (2025) studied Xiaolangdi Dam in China using the SAR images from Sentinel-1, ALOS-1, and ALOS-2 from 2007 to 2023 and discovered decaying settlement of 47 mm/yr (2007–2010) and 25 mm/yr (2015–2023) with the highest deformation of about 42 mm/yr across the dam crest.

Recent research has increasingly employed Deep Learning for predicting InSAR-derived deformation time series. While these efforts have advanced the field, existing methodologies face significant limitations in capturing the spatial dependencies, i.e., correlations among nearby points derived by InSAR processing that frequently exhibit similar deformation behavior due to shared structural or geophysical conditions. One common approach is to employ spatio-temporal K-means clustering to group points derived from InSAR, specifically Point Scatterers (PS) or Distributed Scatterers (DS), and train a separate predictive model for each cluster (Liu et al., 2021; Peng et al., 2024; Xiao et al., 2024). This methodology presupposes homogeneity within clusters. However, it overlooks spatial dependencies, particularly at the boundaries of clusters, thereby neglecting relationships between adjacent points. Additionally, training multiple models for each cluster increases the complexity of hyperparameter optimization and heightens the risk of overfitting, particularly for clusters with limited data points. A second approach simplifies the problem by predicting deformation at a single representative point (Hill et al., 2021; Nava et al., 2023; Zhou et al., 2024). While computationally efficient, this method neglects the spatial dependencies among neighboring points across the study area and cannot provide predictions for all points, limiting its applicability to comprehensive deformation monitoring. A third strategy decomposes the cumulative deformation time series into trend, seasonal, and noise components, predicting trend and seasonal components independently (Zhou et al., 2025). This approach, although detailed, necessitates separate models for each element, thereby increasing computational complexity and model training time. The approaches mentioned above have common limitations: they either oversimplify spatial variability, neglect spatial dependencies, or increase complexity, underscoring the need for a unified framework that integrates spatial and temporal dynamics.

In this study, we propose a novel framework for predicting InSAR-derived dam deformation by combining a Graph Attention Network (GAT) (Veličković et al., 2018) with a Long Short-Term Memory (LSTM) model (Hochreiter and Schmidhuber, 1997), named GAT-LSTM. In particular, the GAT captures the spatial dependencies among nearby points derived from InSAR processing, whereas the LSTM models the temporal variations of deformation time series. This integration allows us to overcome the drawbacks of previous methods without depending on oversimplified assumptions or increasing model complexity. Moreover, GAT-LSTM is designed as a single unified model, while still providing predictions for all points, and avoiding time series decomposition.

2. Site description

Fig. 1 indicates the location of the ORD in the Municipal District of Pincher Creek No. 9, about 10 km north of Pincher Creek in Alberta, Canada. The dam was completed in 1991. It has a crest elevation of 1125.6 m above sea level and an operational reservoir level between 1108 and 1118.6 m, with a maximum storage capacity of 500 million cubic meters (Sharifi and Hendry, 2023). The foundation of the dam is compromised by shear planes within clay shale seams, a common feature in the Western Canadian Sedimentary Basin. Formed by glaciotectonic thrusts and valley rebound due to river erosion, these northwest-to-southeast-oriented shear planes, dipping 0.5° to 1.5° northeast, are weakened to a residual state, reducing their resistance to sliding (Morgenstern, 1989; Davachi et al., 1991). The combination of these geological features can potentially result in instability at the ORD.

3. Datasets

3.1. SAR imagery

We utilized 444 Sentinel-1 images acquired in Interferometric Wide-swath (IW) mode from two ascending (SenAT020 and SenAT122) and one descending (SenDT071) datasets. The C-band Sentinel-1 images were acquired from October 2014 to December 2021 from all three passes, with a spatial resolution of 5 m × 20 m (Range × Azimuth). Fig. 2 illustrates the temporal coverage of three Sentinel-1 SAR datasets. Each

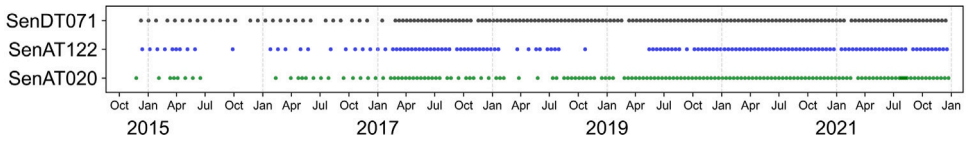

Fig. 2. Temporal availability of Sentinel-1 SAR datasets.

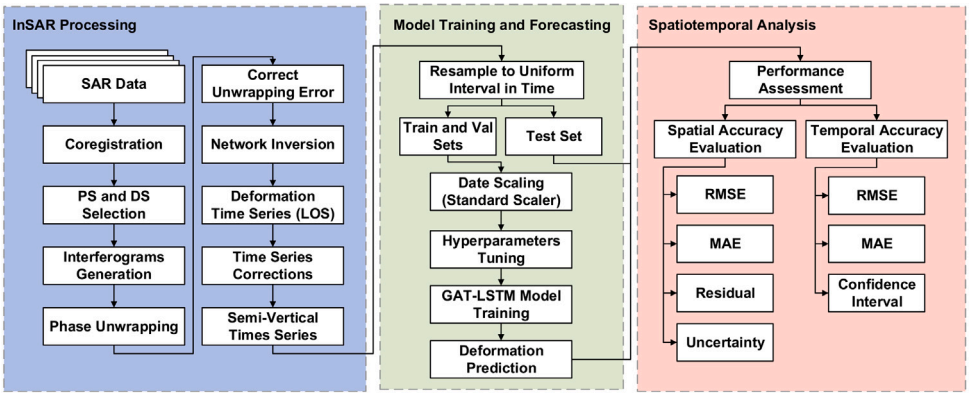

Fig. 3. Workflow of the proposed framework.

dataset is represented by scatter points indicating the presence of valid InSAR measurements on specific dates. Table S1 in the supplementary document provides additional details regarding the datasets.

3.2. Hydrometric data

The Oldman River and its tributaries, the Crowsnest and Castle Rivers, are a key water source of the ORD reservoir. These rivers are monitored by a network of hydrometric stations that capture both discharge and water levels, except for station 05AA032, associated with water levels behind the reservoir (Government of Canada, 2025). Station 05AA022 is adjacent to Castle River, station 05AA008 is positioned along the Crowsnest River, and station 05AA032 is located along the Oldman River (see Fig. 1).

4. Methodologies

Fig. 3 illustrates the overall workflow of the proposed framework, comprising three main steps. Initially, InSAR time series processing is performed to generate deformation time series from Sentinel-1 SAR data. Second, the deformation time series is used to train the proposed model and make predictions. Lastly, a spatiotemporal analysis is conducted to assess the prediction performance. The following subsections provide a detailed description of each step.

4.1. InSAR time series processing

The InSAR Computing Environment (ISCE) Python package (Rosen et al., 2018) was used to generate coregistered single look complexes (SLCs) of the Sentinel-1 ascending and descending datasets. The InSAR time series analysis technique, implemented in MIAmi Phase Linking in Python (MiaplPy) (Mirzaee et al., 2023), was employed, incorporating DS and PS pixels to invert the non-linear time series of deformation. The adopted non-linear phase linking method was eigenvalue decomposition-based maximum likelihood (EMI), specifically sequential EMI, which offers both estimation optimality and computational efficiency (Ansari et al., 2018, 2017). The EMI implementation in MiaplPy follows a combined eigenvalue maximum-likelihood phase linking, named CPL, wherein EMI is the primary phase-linking technique and reverts to the classic eigenvalue decomposition (EVD) for ill-conditioned pixels. A single reference network was considered to generate the interferograms for the Sentinel-1 ascending and descending datasets (Fig. 4). The perpendicular baseline refers to the distance between two satellite acquisitions measured perpendicular to the satellite Line of Sight (LOS) direction. It plays a key role in determining the quality of the interferogram. The average spatial coherence indicates the similarity between radar signals from two acquisitions, reflecting the quality and reliability of the interferometric phase. Higher coherence values suggest more stable measurements for deformation analysis.

In the MiaplPy steps, the self-similar neighbors of each pixel were detected from the SAR image amplitudes via the Anderson–Darling test (Scholz and Stephens, 1987) with a false alarm rate of 5%. PSs and DSs were initially chosen based on the number of self-similar neighbors, with DS pixels exhibiting a count exceeding 10. The complex coherence matrix was computed for each pixel utilizing self-similar neighbors, and the optimal phase history was obtained through phase linking. PS pixels were filtered using the amplitude dispersion index (Ferretti et al., 2001). DS pixels were also filtered using phase-linking temporal coherence. Finally, the optimized phase histories derived from combined DS and PS pixels were utilized to unwrap the interferograms using the Network-Flow Algorithm for Phase Unwrapping (SNAPHU) (Chen and Zebker, 2002, 2001a,b) and invert the displacement time series. It should be noted that the MintPy Python package (Yunjun et al., 2019) is utilized for phase unwrapping error correction, as well as performing deterministic phase corrections on the displacement time series resulting from residual topography, tropospheric, and ionospheric delays. The topographic phase was removed using the 1-arcsecond Shuttle Radar Topography Mission (SRTM) Digital Elevation Model (DEM). The tropospheric delay was corrected using PyAPS (Jolivet et al., 2014, 2011) and the European Centre for Medium-Range Weather Forecasts (ECMWF) Reanalysis v5 (ERA-5) weather model. Regional phase ramps due to long-wavelength tropospheric and ionospheric delays, as well as orbital errors, were also eliminated using a linear ramp computed at each acquisition. Finally, geolocation offsets from DEM errors were corrected using the geolocation correction step in the MiaplPy, following the approach of Fattahi and Amelung (2013) and Jung et al. (2019). It should be noted that a minimum temporal coherence threshold of 0.5 was also adopted following analysis of the coherence maps.

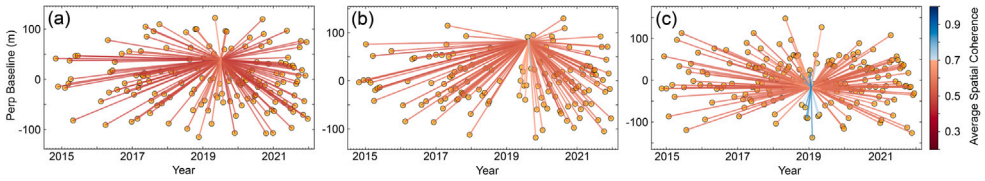

Fig. 4. Networks of interferograms. (a) SenAT020, (b) SenAT122, and (c) SenDT071.

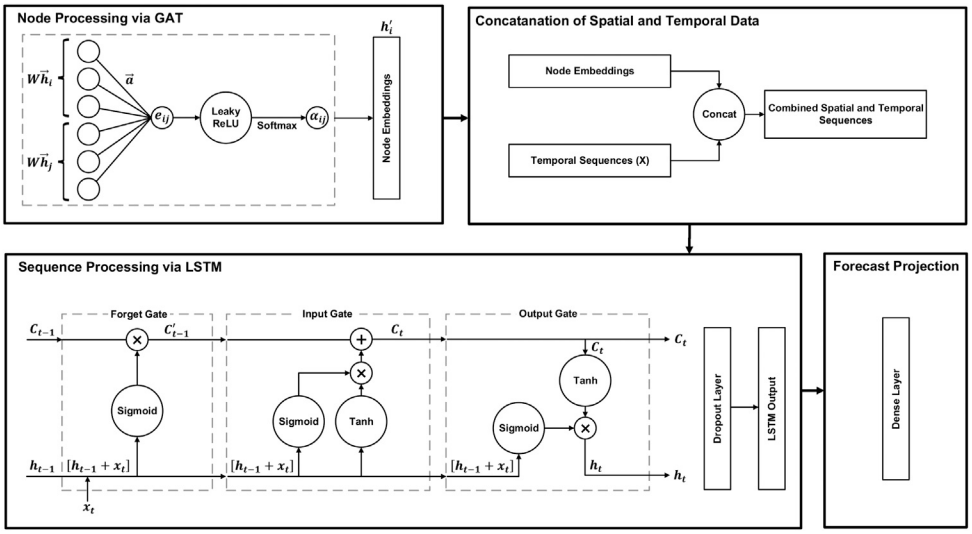

Fig. 5. Workflow of the proposed GAT-LSTM technique. (1) node processing via GAT to capture the spatial dependencies, (2) combining GAT-derived spatial features with temporal deformation sequences, (3) sequence processing via LSTM to model temporal dynamics, and (4) forecast projection, mapping the LSTM output to predict future deformation using a dense layer.

4.2. Proposed spatiotemporal prediction technique

In this study, we proposed a prediction framework based on the GAT and LSTM, which models the spatial dependencies among neighboring InSAR-derived points and integrates them with temporal dependencies to improve the accuracy of InSAR time series forecasting. In the following subsections, each step of the proposed methodology is described sequentially. Fig. 5 illustrates the proposed GAT-LSTM framework.

4.2.1. Graph construction and node feature representation

The spatial relationships among the points are represented as an undirected graph, where each point is a node, and edges connect spatially proximate nodes. The foundation of this graph is the distance matrix, which quantifies the spatial proximity between all pairs of points using their coordinates. The pairwise Euclidean distance matrix was computed for a set of N points with coordinates, serving as the basis for defining the structure of the graph. Then, for each node i, the k closest neighbors are identified using a K Nearest Neighbors technique, excluding the node itself.

Each node contains a feature vector that includes its spatial position and deformation behavior. Spatial coordinates (x_i, y_j) provide explicit positional information. In contrast, deformation statistics, particularly the mean (μ_i) and standard deviation (σ_i) of deformation values across the time steps, summarize the temporal deformation patterns at each point. It should be noted that although these are simple descriptors, their role is limited to providing the GAT with coarse node-level information, and the temporal dynamics will be modeled specifically by the LSTM. Thus, the feature vector for each node i is $\vec{h}_i = [x_i, y_i, \mu_i, \sigma_i]$. To ensure a balanced contribution from each node feature and stabilize training, the node features are also scaled using the Standard Scaler from the Scikit-learn Python package (Pedregosa et al., 2011).

4.2.2. Graph attention network for spatial dependency modeling

To model spatial dependencies among neighboring points derived from InSAR processing, the GAT is employed, which learns node embeddings that encode the spatial context of each point by adaptively weighting the contributions of spatially connected neighbors. The input of a layer is $\mathbf{h} = \{\vec{h}_1, \vec{h}_2, \ldots, \vec{h}_i\}$, and the output of it would be a new set of node features, i.e., $\mathbf{h}' = \{\vec{h}'_1, \vec{h}'_2, \ldots, \vec{h}'_N\}$. A shared linear transformation parameterized by a weight matrix $\mathbf{W}$ is applied to each node to transfer the input features. The key innovation of the GAT is the application of a self-attention mechanism defined by a to compute attention coefficients as $e_{ij} = a(\mathbf{W}\vec{h}_i, \mathbf{W}\vec{h}_j)$, which determine the importance of node j's features to node i.

Here, masked attention is employed to incorporate the graph structure into the attention mechanism, such that e_{ij} is computed for nodes $j \in \mathcal{N}_i$, where $\mathcal{N}_i$ denotes the neighborhood of node i in the graph. Furthermore, the attention mechanism a is a single-layer feedforward neural network, indicated by a weight vector $\vec{\mathbf{a}}$, and applying the LeakyReLU nonlinearity, which is equal to:

$$e_{ij} = \text{LeakyReLU}\left(\vec{\mathbf{a}}^T [\mathbf{W}\vec{h}_i \,\|\, \mathbf{W}\vec{h}_j]\right) \tag{1}$$

where $\|$ denotes concatenation operation and $.^T$ is transposition. To ensure the comparability of the attention coefficients across various nodes and neighborhoods, they are normalized using the softmax function over the neighborhood $\mathcal{N}_i$ as $\alpha_{ij} = \text{softmax}_j(e_{ij})$.

After obtaining the normalized attention coefficients, the output features for the node i are computed as a weighted sum of the transformed features of its neighbors, using the normalized attention coefficients, followed by a nonlinearity σ:

$$\vec{h}'_i = \sigma\left(\sum_{j \in \mathcal{N}_i} \alpha_{ij} \mathbf{W}\vec{h}_j\right) \tag{2}$$

To stabilize the learning process and increase the capacity of the model, multi-head attention is employed (Vaswani et al., 2017). Here, K independent attention mechanisms are applied, each with its weight matrix $\mathbf{W}^k$ and attention coefficients α_{ij}^k. The outputs of these heads are concatenated to form the intermediate representation:

$$\vec{h}_i' = \Big\Vert_{k=1}^{K} \sigma\left(\sum_{j\in\mathcal{N}_i} \alpha_{ij}^k \mathbf{W}^k \vec{h}_j\right), \tag{3}$$

where $\|$ denotes concatenation, α_{ij}^k are the normalized attention coefficients for the kth head, computed similarly to the single-head case, and $\mathbf{W}^k$ is the weight matrix for the kth head. However, for the final layer, concatenation is no longer appropriate, and the outputs of the attention heads are computed using average as follows:

$$\vec{h}_i' = \sigma\left(\frac{1}{K}\sum_{k=1}^{K}\sum_{j\in\mathcal{N}_i} \alpha_{ij}^k \mathbf{W}^k \vec{h}_j\right). \tag{4}$$

Regularization techniques are integrated into each GAT layer to mitigate overfitting and stabilize the training process. Specifically, dropout is applied for regularization. Additionally, L2 regularization is imposed on the kernel weights and attention parameters. The final output represents the learned spatial embeddings for each of the N points. This ensures that the resulting node embeddings h' capture the spatial relationships among points for subsequent temporal modeling.

4.2.3. Long short-term memory for temporal dependency modeling

The spatial representations derived from the GAT are integrated with the temporal sequences to form enriched input data for the LSTM. This integration bridges the node embeddings derived from the GAT with the temporal dynamics, which the LSTM will model to perform the deformation forecasting task. Sequence construction is parameterized by two variables: n_{past}, the number of past time steps used as input, and n_{future}, the number of future time steps to predict. For a dataset comprising T time steps and N spatial points, the sequence creation process generates input-target pairs (X, y). Here, X represents the input sequences capturing past observations, and y denotes the target sequences for future predictions. For each sequence s at point i, the GAT output $\vec{h}_i'$ is a static spatial embedding reflecting the relationships of the node with its neighbors. To align this spatial feature with the temporal dimension of the sequences, $\vec{h}_i'$ is expanded across the n_{past} time steps by replication. The expanded GAT features are then concatenated with the sequences created from the InSAR deformation time series.

The LSTM processes sequential data at each time step t, utilizing the current input x_t and the previous hidden state h_{t-1} (Peixeiro, 2022). The LSTM consists of three gates: the forget gate, the input gate, and the output gate. The forget gate determines which information from the previous cell state C_{t-1} should be discarded. The sigmoid function produces outputs ranging from 0 to 1, where zero indicates that the information is discarded. In contrast, one means it is fully retained. Intermediate values also determine the proportion of information to be forgotten or retained. This forget vector is then multiplied elementwise with the previous cell state C_{t-1} to produce an intermediate cell state C'_{t-1}, representing the filtered information after forgetting. The input gate introduces new information into the cell state, consisting of two components: an input activation gate computed via a sigmoid function, and a candidate cell state computed via a tanh function. The sigmoid function determines parts of new information to be retained, while the tanh function scales the input to a range of $[-1, 1]$ for computational efficiency. The output of the two components is combined through elementwise multiplication and then added to C'_{t-1} to produce the updated cell state C_t. The output gate controls the exposure of the internal cell state C_t to the next hidden state h_t, containing a sigmoid gate that determines those parts of the cell state that influence the output. The hidden state is then calculated as the elementwise multiplication of sigmoid and tanh outputs. This operation produces the new hidden state h_t, which contains information relevant to the current input and the previous context.

It should be noted that regularization is applied across the LSTM architecture to mitigate overfitting, and dropout is incorporated after each LSTM layer. The final hidden state captures the learned temporal representation, which is then passed through a dense layer that maps this representation to the target output at the next time step. Finally, the LSTM model is compiled using the Adam optimizer, with the training objective focused on minimizing the Huber loss function (Huber, 1964), which balances sensitivity to outliers and robustness to noise. Two primary callbacks, namely early stopping and learning rate reduction on the plateau, were also employed, each designed to optimize the convergence and performance of the model.

5. Results

5.1. Deformation analysis of the ORD

5.1.1. Spatial pattern of deformation

Given the availability of both ascending and descending InSAR results, we performed a horizontal (east–west) and vertical decomposition of the LOS velocities. For this purpose, we resampled the velocities and their geometries into a uniform 20-meter grid using nearest neighbor interpolation (Wright et al., 2004) to align the irregularly distributed InSAR-derived points from the ascending and descending passes, which do not coincide spatially.

Fig. 6 shows the LOS and decomposed horizontal and vertical velocities, revealing that the horizontal deformation rates and patterns are negligible. Consistency assessment between the three InSAR results is provided in section S1 of the supplementary document. The absence of significant horizontal deformation in the decomposed velocity can be attributed to the geometric alignment of the dam relative to the orbital path of the Sentinel-1 satellite. Sentinel-1 operates in a near-polar orbit, making it sensitive to motion in the LOS direction, which combines vertical and east–west horizontal displacement components. However, it has limited sensitivity to north-south horizontal displacement due to the steep inclination of the satellite. Because the ORD is oriented predominantly north-south, horizontal displacements occurring along the axis of the dam (i.e., in the north-south direction) are less detectable in the LOS measurements, while vertical and east–west components are more readily observed. Acknowledging this, a comprehensive analysis of north-south deformation is not feasible with the current Sentinel-1 data alone and is beyond the scope of this study. Specifically, the crest of the dam exhibited significant subsidence, as evidenced in the decomposed vertical velocity components. Given these structural and geometric constraints and observing noticeable vertical subsidence along the dam crest, this study primarily focuses on semi-vertical velocities to analyze the structural changes of the dam. The standard method for estimating semi-vertical ground deformation involves dividing the InSAR LOS measurement (v_{LOS}) by the cosine of the incidence angle (θ), assuming negligible horizontal ground motion, i.e., $v_{sv} = v_{LOS}/\cos(\theta)$ (Hung et al., 2011; Hu et al., 2014).

Fig. 7 demonstrates the semi-vertical deformation velocities derived from SenAT020, SenDT122, and SenDT071. The semi-vertical velocity maps for all three datasets consistently illustrated a pattern of deformation concentrated along the crest of the dam, with maximum subsidence rates of 5.85 mm/yr, 6.23 mm/yr, and 5.08 mm/yr for the SenAT020, SenAT122, and SenDT071 datasets, respectively. The negative deformation rates confirmed that the dam crest is experiencing subsidence, which is consistent across all three datasets. Figure S4 of the supplementary document illustrates the velocity standard deviation maps, which denote measurement uncertainty, with lower values corresponding to lower measurement uncertainty.

It should be noted that we utilized semi-vertical time series data for the subsequent application of the GAT-LSTM model to predict deformation trends. The semi-vertical decomposition uses the LOS velocities directly from individual tracks (SenAT020, SenAT122, and SenDT071). In

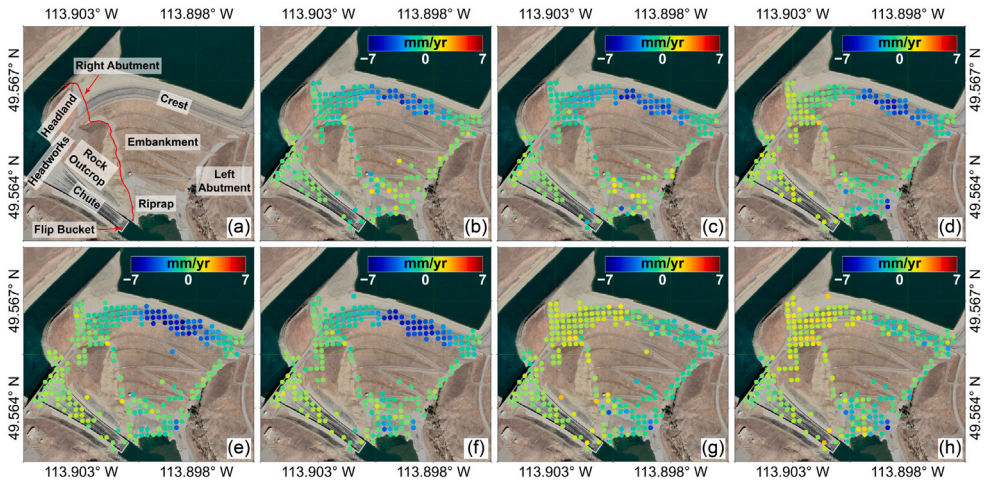

Fig. 6. The LOS and decomposed velocities of ORD. (a) overview of ORD and its components (Sharifi and Hendry, 2023), (b)–(d) LOS velocities for SenAT020, SenAT122, and SenDT071, respectively. (e)–(f) decomposed vertical components, incorporating SenAT020 and SenDT071, and SenAT122 and SenDT071, respectively. (g)–(h) decomposed horizontal components from SenAT020 and SenDT071, and SenAT122 and SenDT071, respectively.

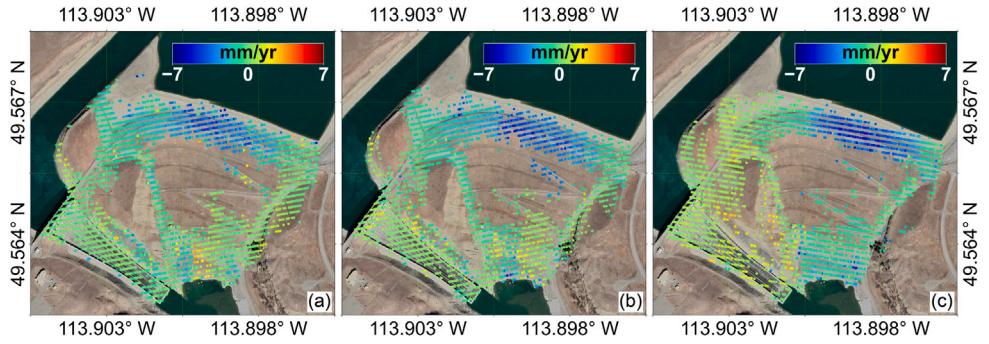

Fig. 7. Semi-vertical velocities. (a) SenAT020, (b) SenAT122, and (c) SenDT071.

contrast, horizontal-vertical decomposition requires temporally aligning the time series from one pass (for instance, SenAT020) with another (for example, SenDT071) to ensure a consistent 12-day interval. Achieving this alignment necessitates temporal interpolation of one dataset to match the temporal distribution of the other, effectively generating synthetic InSAR data. Moreover, the significant temporal gaps in both ascending tracks further introduce manipulated data. Following temporal interpolation, a gridding step becomes necessary to align the corresponding points. These various steps may introduce errors that could compromise the reliability of the InSAR time series for GAT-LSTM training. In contrast, the semi-vertical approach utilizes the LOS data without such manipulations, thereby preserving the integrity of the original measurements and fully exploiting the spatial resolution of the points. Considering the minimal horizontal deformation observed and the practical challenges associated with interpolation and gridding, we conclude that the semi-vertical time series constitutes a more robust option for GAT-LSTM model training and prediction in this context

5.1.2. Temporal pattern of deformation

Fig. 8 illustrates the water level behind the dam, alongside the InSAR-derived mean cumulative semi-vertical deformation on the dam crest, and the trend line to assess the relationship between the reservoir water levels and the dam crest stability. Similar studies analyzed the relation between the reservoir level and InSAR deformation. For instance, at the ORD, average LOS displacements of InSAR-derveid points on the headworks follow reservoir fluctuations with a lagged response (Sharifi and Hendry, 2023); at the Mosul Dam, InSAR deformations had an inverse relation to reservoir level, i.e., subsidence decreases when water level increases (Othman et al., 2019); at Xe Pian–Xe Namnoy (Saddle Dam D), water loading explained more than half of the displacement at certain monitoring points, highlighting significant water-induced deformation (Xie et al., 2022a), and at the Sardoba Dam, the seasonal fluctuations showed that both vertical and horizontal east–west displacements were uncorrelated with reservoir water level and temperature variations (Xie et al., 2022b).

Between mid-2017 and early 2019, a significant decrease in water levels was recorded, resulting in a minimum water level during this period. A reduced water level lowers the hydrostatic pressure applied to the upstream slope of the dam, i.e., the face in direct contact with the reservoir water. Although it may initially appear advantageous for dam stability, it can result in a phenomenon known as reservoir drawdown-induced deformation, which occurs when the upstream slope of the dam experiences a rapid reduction of the water level (Pinyol et al., 2008). Two main effects arise in such cases: the stabilizing hydrostatic pressure on the upstream slope is reduced, and the internal pore-water pressures within the dam are modified, potentially creating critical conditions for slope stability (Pinyol et al., 2008). One possible explanation for the observed acceleration during this period might be related to the reduction in water load, which altered the stress distribution within the dam body, leading to a temporary increase in deformation rates along the crest. Consequently, the slope of the second segment (S2) of the deformation trend indicates an increase in the deformation rate during this period, consistent with a drawdown-related response. However, this interpretation should be considered a plausible explanation rather than a formally tested hypothesis.

The water level began to recover in 2019. During 2020 and 2021, the deformation rate of the S3 segment demonstrated a decreased slope,

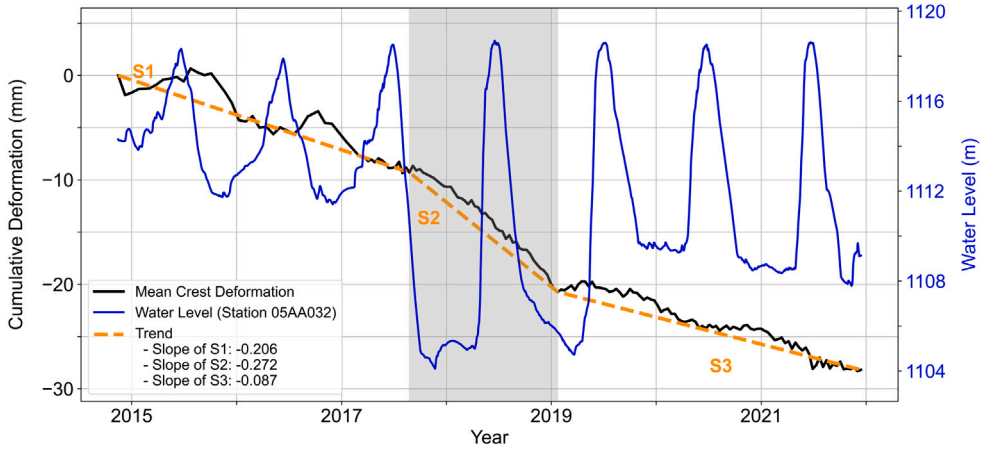

Fig. 8. Mean crest cumulative deformation derived from semi-vertical SenDT071 vs. reservoir water level. The breakpoints in the deformation trend are subsequently identified utilizing the ruptures Python package (Truong et al., 2020). A three-segment trend line is applied to the mean crest time series deformation, and the slopes of each segment are calculated.

indicating a deceleration in the deformation rate compared to the S2 segment. This might suggest that the increasing water level partially stabilizes the dam crest by restoring a more balanced stress condition within the structure. However, the deformation rate remains negative, indicating that the dam is experiencing subsidence, albeit at a reduced rate. This persistent deformation may be attributed to the irreversible changes in the material characteristics of the dam that occurred during the previous drawdown phase. It should be noted that atmospheric and orbital errors can potentially introduce long-wavelength artifacts in InSAR time series. In this study, these effects were mitigated through a multi-step correction strategy, including tropospheric delay correction using PyAPS with ERA-5, deterministic ramp and residual topography corrections in MintPy, and phase-linking in MiaplPy to suppress noise propagation. Moreover, the consistency of the deformation between ascending and descending tracks (see supplementary document) supports the interpretation that the observed acceleration likely reflects a deformation process rather than an atmospheric artifact. However, we acknowledge that the lack of independent ground-based measurements limits our ability to validate these interpretations directly. This limitation is typical for critical infrastructure, like dams, where access to in-situ data may be restricted.

5.2. Deformation prediction using GAT-LSTM

5.2.1. Data preparation

The dataset utilized for the prediction task contains time-series semi-vertical deformation measurements derived from InSAR observations, specifically the SenDT071 dataset. The dataset includes 147 dates from February 26, 2017, to December 14, 2021, and contains 2506 points over the ORD derived from joint PS and DS InSAR processing. This particular time frame was deliberately selected to omit prior periods in the dataset that exhibited substantial data gaps. To address the minor gaps within the chosen interval, linear interpolation was used to align the data with the 12-day temporal resolution of the Sentinel-1 satellite.

The time series data is split into training, validation, and test sets for model development and assessment. The test set consisted of the last 10 dates from August 28, 2021, to December 14, 2021, exclusively designated to assess the capability of the model to generalize to unseen data. The training set includes 117 dates from February 26, 2017, to December 19, 2020, whereas the validation set contains 20 dates (December 31, 2020, to August 16, 2021). Given that the deformation data encompassed both positive and negative values, the Standard Scaler was applied exclusively to the training set to prevent data leakage.

Table 1
Optimal hyperparameters of the GAT-LSTM tuned using Optuna.

Category	Hyperparameter	Values
General	Batch size	2048
	Epochs	128
	n_{past}	15
	n_{future}	1
LSTM	Architecture	32 units, 1 layer
	Dropout	0.4 (after an LSTM layer)
	Learning rate	0.001
GAT	Architecture	16 units, 1 layer
	Attention heads	4
	K neighbors	16
	Dropout	0.1
Regularization	L2 regularization (LSTM and GAT)	0.003

5.2.2. Hyperparameter tuning

The hyperparameter optimization for the GAT-LSTM model was performed utilizing the Optuna Python package (Akiba et al., 2019) to determine optimal parameter configurations effectively. Optuna utilizes a Bayesian optimization approach, specifically the Tree-structured Parzen Estimator (TPE) algorithm, to investigate the hyperparameter space. The tuned hyperparameters are reported in Table 1.

5.2.3. Spatial prediction performance evaluation

The model was independently trained ten times to account for the inherent randomness in Deep Learning models introduced by random weight initialization, stochastic gradient descent, dropout regularization, and random mini-batch sampling. The average Root Mean Square Error (RMSE), Mean Absolute Error (MAE), and their standard deviations are reported to ensure a robust evaluation. Forecasts were generated through a recursive process. Specifically, the model predicted the next time step, appended the resultant value to the sequence, and used it as input for the subsequent prediction. Model predictions were evaluated against InSAR-derived ground-truth deformation measurements, allowing for a quantitative performance assessment.

Figs. 9 and 10 illustrate the GAT-LSTM predictions from August 28 to December 14, 2021, organized into four columns across ten dates: observed InSAR deformation, mean predicted deformation, mean residual maps, and the corresponding uncertainty, computed based on the standard deviation of each predicted point across ten independent model runs. It should be noted that since ORD is a slow-moving dam, the deformation patterns along the ten dates appear to be constant. Nevertheless, the residual maps offer an additional, more discerning

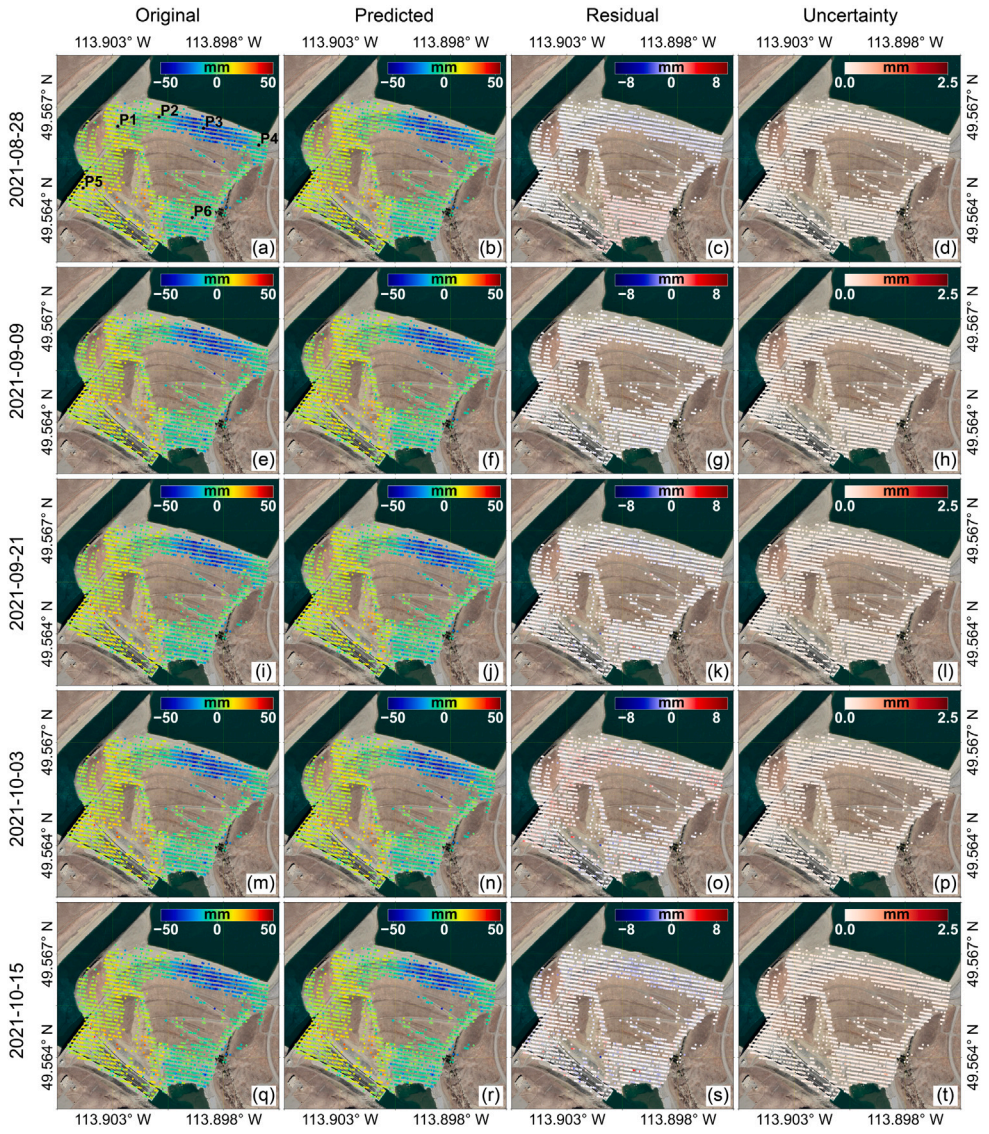

Fig. 9. Spatial distribution of predicted points based on the GAT-LSTM model over ORD from 2021-08-28 to 2021-10-15. From left to right, original deformation maps, predicted mean deformation maps, mean residual maps, and uncertainty maps.

layer of evaluation. As can be seen, the prediction error and uncertainty accumulate progressively over time, resulting in higher levels of error and uncertainty at the final forecasted date. By contrast, the LSTM model (Figures S2 and S3 in the supplementary document) demonstrated more erratic and spatially clustered residuals, particularly along the dam crest, highlighting the limitations of the LSTM model, which relies solely on temporal dynamics. Conversely, the GAT-LSTM model significantly improves prediction accuracy by utilizing a graph attention mechanism. Importantly, the temporal increase in uncertainty does not lead to severe spatial instability and remains low in structurally sensitive areas, particularly along the crest.

Table 2 compares the performance of the GAT-LSTM and LSTM models for deformation prediction on the unseen test set, using RMSE and MAE as evaluation metrics. Across all test dates, GAT-LSTM consistently outperformed LSTM, yielding lower error values in both metrics. While accuracy remains the primary metric for evaluating model performance, standard deviation offers additional insight into model stability. In this regard, GAT-LSTM demonstrated greater consistency. Both models, however, consistently showed a trend of increasing prediction error with time. As shown in Table 2, the RMSE and MAE values for both techniques increase towards the last date, particularly for the LSTM model. Although GAT-LSTM also witnesses a drift of error over time, the increase was comparatively smaller. This is mainly due to the recursive approach used for forecasting, which leads to error accumulation over time.

5.2.4. *Temporal prediction performance evaluation*

To evaluate the temporal precision of the deformation predictions for the ORD, the accuracy of the GAT-LSTM and LSTM models was investigated at six strategically chosen locations throughout the dam structure, as illustrated in Fig. 9. Figs. 11 and 12 represent the time series of InSAR-derived deformations along with the predictions from the GAT-LSTM and LSTM models, respectively. The 95% confidence intervals are included to quantify the uncertainty in the predictions. An in-depth analysis of Figs. 11 and 12 indicates that the GAT-LSTM model generally outperforms the LSTM model in terms of RMSE and MAE, demonstrating its enhanced capacity to capture the temporal dynamics of dam deformation. At locations exhibiting complex deformation patterns, such as P3, situated on the crest, the GAT-LSTM outperforms the LSTM significantly.

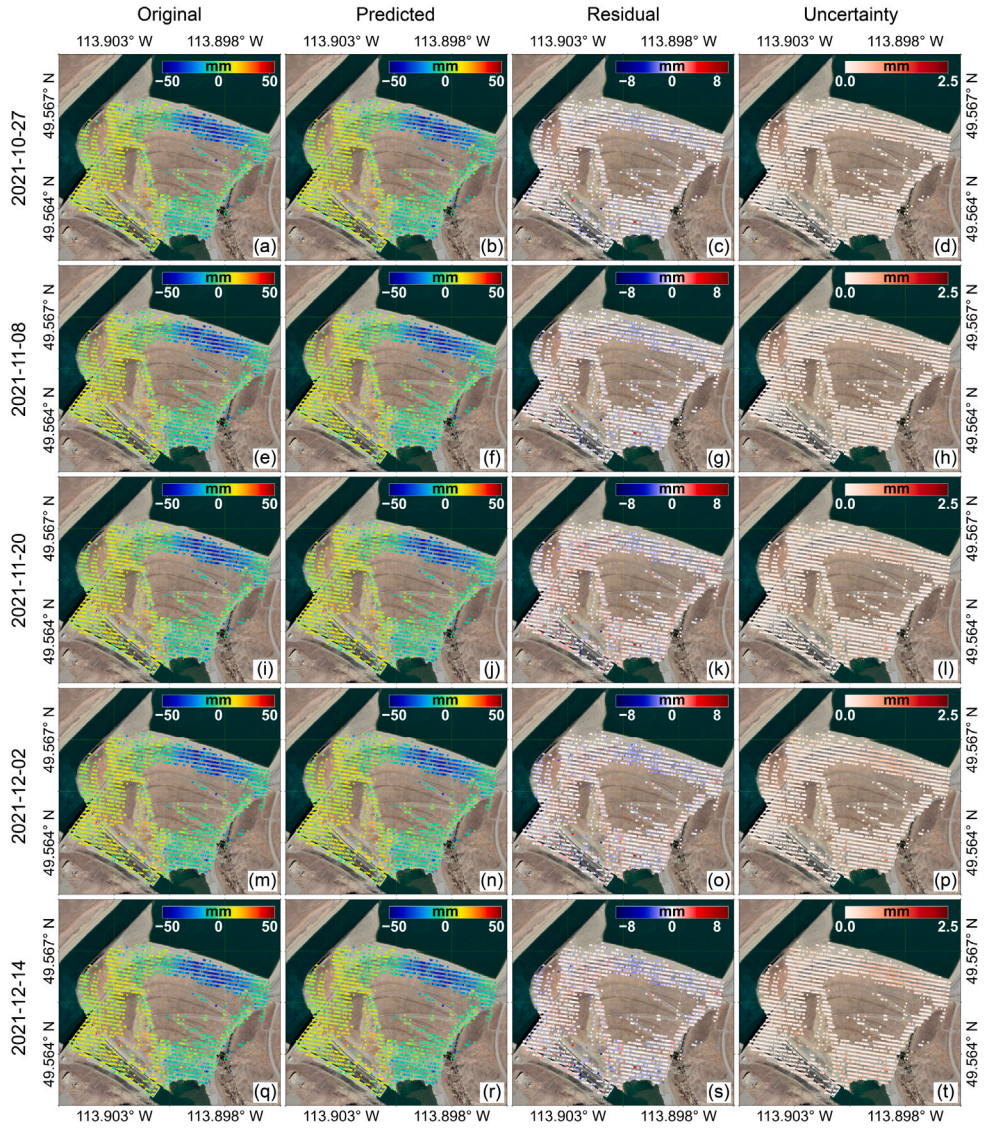

Fig. 10. Spatial distribution of predicted points based on the GAT-LSTM model over ORD from 2021-10-27 to 2021-12-14. From left to right, original deformation maps, predicted mean deformation maps, mean residual maps, and uncertainty maps.

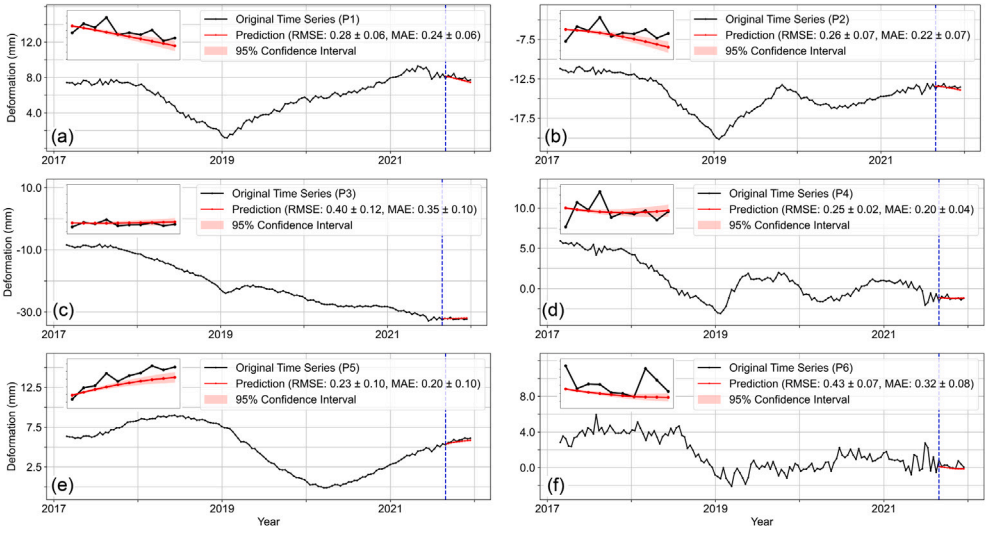

Fig. 11. Cumulative time series prediction results based on the GAT-LSTM technique for six points selected on different parts of the dam.

Table 2
Accuracy assessment of prediction based on the LSTM and GAT-LSTM techniques for 10 dates (unit is mm).

		2021-08-28	2021-09-09	2021-09-21	2021-10-03	2021-10-15
LSTM	RMSE	0.47 ± 0.022	0.34 ± 0.030	0.46 ± 0.050	0.66 ± 0.042	0.78 ± 0.088
	MAE	0.39 ± 0.015	0.26 ± 0.026	0.33 ± 0.036	0.51 ± 0.039	0.53 ± 0.058
GAT-LSTM	RMSE	0.45 ± 0.016	0.30 ± 0.013	0.39 ± 0.014	0.64 ± 0.023	0.61 ± 0.032
	MAE	0.37 ± 0.014	0.22 ± 0.012	0.28 ± 0.013	0.49 ± 0.020	0.43 ± 0.028
		2021-10-27	2021-11-08	2021-11-20	2021-12-02	2021-12-14
LSTM	RMSE	0.90 ± 0.104	1.05 ± 0.124	1.18 ± 0.138	1.34 ± 0.172	1.44 ± 0.192
	MAE	0.63 ± 0.074	0.74 ± 0.088	0.88 ± 0.100	0.94 ± 0.113	1.02 ± 0.135
GAT-LSTM	RMSE	0.72 ± 0.035	0.83 ± 0.043	0.98 ± 0.035	1.03 ± 0.052	1.10 ± 0.061
	MAE	0.51 ± 0.032	0.60 ± 0.039	0.73 ± 0.029	0.74 ± 0.044	0.80 ± 0.054

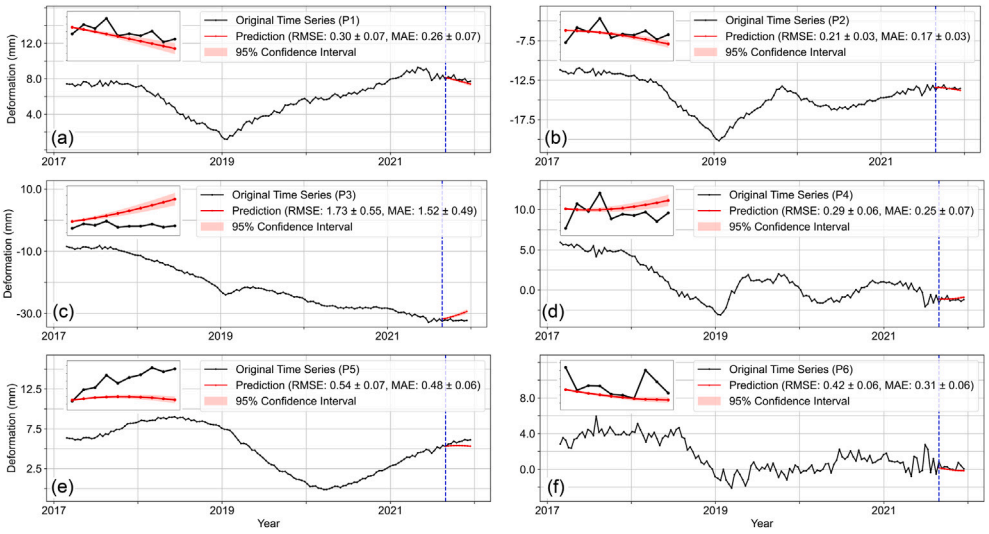

Fig. 12. Cumulative time series prediction results based on the LSTM technique for six points selected on different parts of the dam.

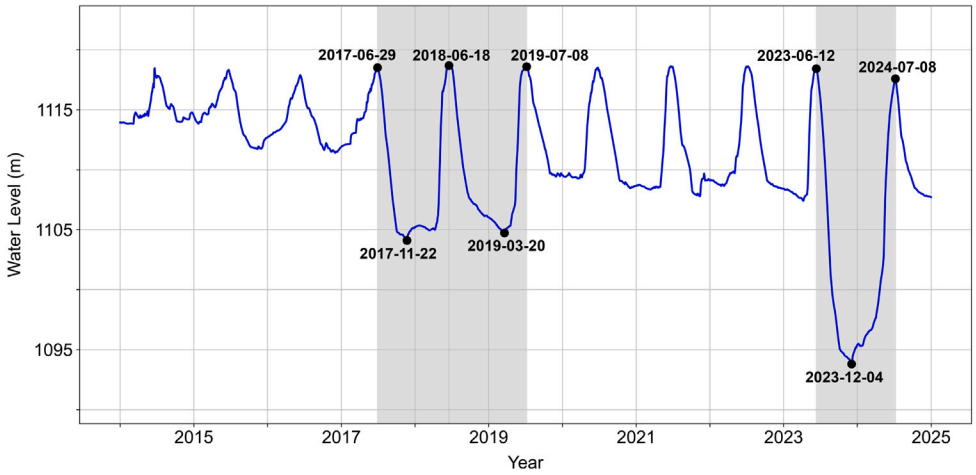

Fig. 13. Water level time series recorded by the station 05AA032 from 2014 to 2025.

6. Discussions

6.1. Water level changes in subsequent years

Fig. 13 shows the water level related to the ORD from 2015 to the end of 2024, recorded by Station 05AA032. Between mid-2017 and mid-2019, the water level experienced two significant low levels. A severe decline in water level is observed at the end of 2023. This event surpasses the magnitude of the 2017–2019 drawdowns, suggesting a heightened potential for structural impact. The prolonged reduction in water load during this period could further exacerbate consolidation processes, such as increased and accelerated subsidence on the dam crest due to the altered stress within the dam. However, the severity of this recent hydrological event must be investigated using recent InSAR data or other dam monitoring techniques.

6.2. Spatial reliability analysis of LSTM and GAT-LSTM models

This subsection aims to assess the reliability of the LSTM and GAT-LSTM models in a short-term forecasting scenario to mitigate the error

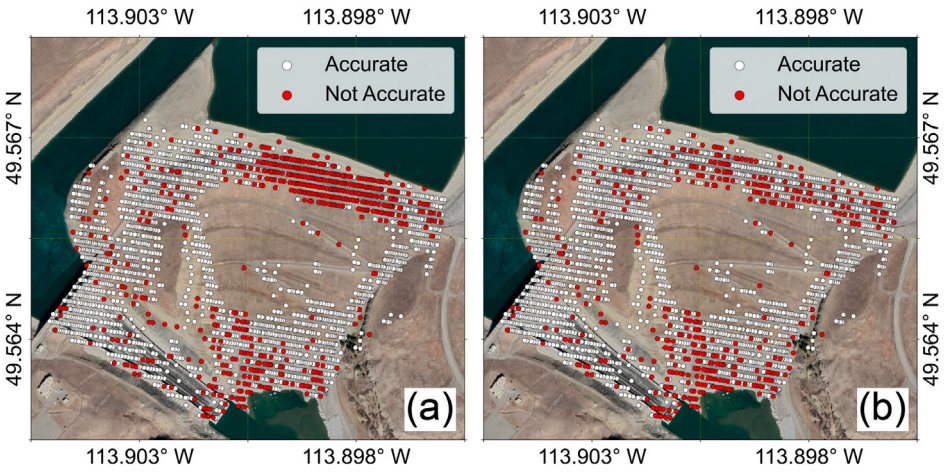

Fig. 14. Spatial distribution of prediction accuracy for short-term 36-day deformation forecasting using (a) LSTM and (b) GAT-LSTM.

accumulation inherent in recursive prediction. A stringent accuracy threshold of 0.5 mm was established for both RMSE and MAE metrics to ensure alignment with the sub-millimeter precision required for dam deformation monitoring. For each point, the mean RMSE and MAE standard error were calculated as the standard deviation across the ten repeats divided by the square root of the sample size of ten. The upper bound of the 95% confidence interval for each metric was then determined using a t-distribution with nine degrees of freedom. A point was determined as accurate only if the upper bounds of both RMSE and MAE confidence intervals were below the 0.5 mm threshold, reflecting the stringent precision demands of dam monitoring applications. The results indicate that GAT-LSTM outperforms LSTM in short-term forecasting. GAT-LSTM achieved a proportion of accurate points of 83.64% (2096 out of 2506), compared to 76.90% for LSTM (1927 out of 2506). This improvement of 6.74 percentage points underscores the advantage of the GAT-LSTM technique over the LSTM.

Fig. 14 shows the distribution of prediction reliability across the ORD. For LSTM, a high concentration of inaccurate predictions is observed along the dam crest. The conventional LSTM captures only temporal dependencies and therefore cannot capture the spatially correlated deformation behavior characteristic of the dam crest. In contrast, the GAT-LSTM incorporates these spatial dependencies among nearby points throughout the dam structure, enabling the model to predict deformation more accurately. The higher concentration of inaccurate predictions derived by the LSTM technique along the crest can thus be explained by its lack of spatial context. Moreover, the recursive prediction strategy employed by both models leads to error accumulation as the forecast horizon increases, although this effect is mitigated in the GAT-LSTM.

7. Conclusions

This study introduces a novel framework for dam deformation prediction by integrating graph attention networks with the long short-term memory model (GAT-LSTM) applied to InSAR-derived deformation data from the Oldman River Dam in Alberta, Canada. By addressing the limitations of prior approaches, such as neglecting spatial dependencies and increasing model complexity through InSAR-derived points clustering or time series decomposition, the proposed GAT-LSTM model captures spatial and temporal dynamics of deformation across the entire study area, enhancing predictive accuracy for operational monitoring. The InSAR analysis revealed consistent subsidence along the dam crest, with maximum semi-vertical subsidence rates ranging from 5.08 to 6.23 mm/yr across three Sentinel-1 passes. A significant finding was the accelerated crest deformation between mid-2017 and early 2019, driven by reservoir drawdown, with the deformation rate decelerating as water levels recovered through 2021. However, a severe decline in water levels at the end of 2023 suggests a potential for renewed deformation acceleration, underscoring the need for ongoing monitoring. The GAT-LSTM model outperformed the standard LSTM in forecasting over the last 10 dates of the time series, achieving lower RMSE and MAE values, with the best performance on September 9, 2021 (RMSE of 0.30 ± 0.013 mm and MAE of 0.22 ± 0.012 mm). Notably, GAT-LSTM achieved 83.64% accurate points compared to 76.90% for LSTM, with improved reliability along the dam crest, a critical area for structural stability. The findings would have significant implications for dam safety and infrastructure monitoring, particularly in the Canadian context, where InSAR-based studies remain limited. The GAT-LSTM framework can provide a reliable tool for short-term forecasting (e.g., 36-day horizons), which aligns with operational planning cycles and minimizes error accumulation, making it actionable for dam management.

Despite its predictive capabilities, the GAT-LSTM technique has limitations, primarily stemming from its recursive nature and exclusion of exogenous variables. The recursive prediction process results in the accumulation of errors as the forecast horizon increases. Moreover, neglecting exogenous variables may limit the capacity of the model to incorporate the influence of external factors on deformation prediction. Integrating external variables within a recursive framework would be challenging, as it necessitates the simultaneous prediction of both deformation and external features. In our future work, we will enhance the predictive framework to address the issue of error accumulation and effectively integrate exogenous features. To overcome these limitations, the GAT-LSTM framework can be extended into a sequence-to-sequence (Seq2Seq) architecture (Sutskever et al., 2014), enabling the model to predict the entire future sequence non-recursively and allowing for the integration of exogenous features into the model. Finally, with the recent availability of Sentinel-1C data, incorporating these observations into InSAR processing lies beyond the scope of this study. As Sentinel-1C accumulates acquisitions, our future work will integrate these data to extend the deformation time series and assess whether the subsidence patterns observed on the dam crest persist.

CRediT authorship contribution statement

Ramin Farhadiani: Writing – original draft, Visualization, Methodology, Investigation, Formal analysis, Data curation, Conceptualization. **Sayyed Mohammad Javad Mirzadeh:** Writing – review & editing, Formal analysis, Data curation, Conceptualization. **Ehsan Roshani:** Writing – review & editing, Supervision, Project administration. **Daniel Cusson:** Writing – review & editing. **Saeid Homayouni:** Writing – review & editing, Supervision, Resources, Project administration, Funding acquisition.

Declaration of competing interest

The authors declare that they have no known competing financial interests or personal relationships that could have appeared to influence the work reported in this paper.

Acknowledgments

The authors acknowledge the Copernicus program for providing open access to Sentinel-1 data and the digital research infrastructure provided by Alliance Canada, which was instrumental in supporting the hyperparameter tuning experiments conducted in this study. Furthermore, the GAT-LSTM model was implemented using the TensorFlow (Abadi et al., 2016), Spektral (Grattarola and Alippi, 2021), and Optuna (Akiba et al., 2019) Python packages. This work was also supported by the National Research Council of Canada's Digital Health and Geospatial Analytics (DHGA) program, grant number DHGA-124-1 and Climate Resilient Build Environment Program. The authors would also like to express their sincere gratitude to Dr. Sara Mirzaee for the detailed responses to the authors' technical inquiries regarding MiaplPy package.

Appendix A. Supplementary data

Supplementary material related to this article can be found online at https://doi.org/10.1016/j.jag.2025.104968.

Data availability

Data will be made available on request.

References

Abadi, M., Barham, P., Chen, J., Chen, Z., Davis, A., Dean, J., Devin, M., Ghemawat, S., Irving, G., Isard, M., Kudlur, M., Levenberg, J., Monga, R., Moore, S., Murray, D.G., Steiner, B., Tucker, P., Vasudevan, V., Warden, P., Wicke, M., Yu, Y., Zheng, X., 2016. TensorFlow: A system for large-scale machine learning. In: Proceedings of the 12th USENIX Symposium on Operating Systems Design and Implementation (OSDI 2016), Savannah, GA, USA. pp. 265–283. http://dx.doi.org/10.48550/arXiv.1605.08695.

Akiba, T., Sano, S., Yanase, T., Ohta, T., Koyama, M., 2019. Optuna: A next-generation hyperparameter optimization framework. In: Proceedings of the ACM SIGKDD International Conference on Knowledge Discovery and Data Mining. pp. 2623–2631. http://dx.doi.org/10.1145/3292500.3330701.

Ansari, H., De Zan, F., Bamler, R., 2017. Sequential estimator: Toward efficient InSAR time series analysis. IEEE Trans. Geosci. Remote Sens. 55 (10), 5637–5652. http://dx.doi.org/10.1109/TGRS.2017.2711037.

Ansari, H., De Zan, F., Bamler, R., 2018. Efficient phase estimation for interferogram stacks. IEEE Trans. Geosci. Remote Sens. 56, 4109–4125. http://dx.doi.org/10.1109/TGRS.2018.2826045.

Chen, C.W., Zebker, H.A., 2001a. Network approaches to two-dimensional phase unwrapping: Intractability and two new algorithms: Erratum. J. Opt. Soc. Amer. A 18, http://dx.doi.org/10.1364/josaa.18.001192, 1192–1192.

Chen, C.W., Zebker, H.A., 2001b. Two-dimensional phase unwrapping with use of statistical models for cost functions in nonlinear optimization. J. Opt. Soc. Amer. A 18, 338–351. http://dx.doi.org/10.1364/josaa.18.000338.

Chen, C.W., Zebker, H.A., 2002. Phase unwrapping for large SAR interferograms: Statistical segmentation and generalized network models. IEEE Trans. Geosci. Remote Sens. 40, 1709–1719. http://dx.doi.org/10.1109/TGRS.2002.802453.

Davachi, M.M., Sinclair, B.J., Hartmaier, H.H., Baggott, B.L., Peters, J.E., 1991. Determination of the Oldman river dam foundation shear strength. Can. Geotech. J. 28, 698–707. http://dx.doi.org/10.1139/t91-084.

Fattahi, H., Amelung, F., 2013. DEM error correction in InSAR time series. IEEE Trans. Geosci. Remote Sens. 51 (7), 4249–4259. http://dx.doi.org/10.1109/TGRS.2012.2227761.

Ferretti, A., Prati, C., Rocca, F., 2001. Permanent scatterers in SAR interferometry. IEEE Trans. Geosci. Remote Sens. 39, 8–20. http://dx.doi.org/10.1109/36.898661.

Government of Canada, 2025. Historical hydrometric data. https://wateroffice.ec.gc.ca/mainmenu/historical_data_index_e.html.

Grattarola, D., Alippi, C., 2021. Graph neural networks in TensorFlow and Keras with spektral [application notes]. IEEE Comput. Intell. Mag. 16, 78–87. http://dx.doi.org/10.1109/MCI.2020.3039072.

Hill, P., Biggs, J., Ponce-López, V., Bull, D., 2021. Time-series prediction approaches to forecasting deformation in sentinel-1 InSAR data. J. Geophys. Res. Solid Earth 126, e2020JB020176. http://dx.doi.org/10.1029/2020JB020176.

Hochreiter, S., Schmidhuber, J., 1997. Long short-term memory. Neural Comput. 9, 1735–1780. http://dx.doi.org/10.1162/neco.1997.9.8.1735.

Hu, J., Li, Z.W., Ding, X.L., Zhu, J.J., Zhang, L., Sun, Q., 2014. Resolving three-dimensional surface displacements from InSAR measurements: A review. Earth Sci. Rev. 133, 1–17. http://dx.doi.org/10.1016/j.earscirev.2014.02.005.

Hu, X., Oommen, T., Lu, Z., Wang, T., Kim, J.-W., 2017. Consolidation settlement of Salt Lake county tailings impoundment revealed by time-series InSAR observations from multiple radar satellites. Remote Sens. Environ. 202, 199–209. http://dx.doi.org/10.1016/j.rse.2017.05.023.

Huber, P.J., 1964. Robust estimation of a location parameter. Ann. Math. Stat. 35, 73–101. http://dx.doi.org/10.1214/aoms/1177703732.

Hung, W.C., Hwang, C., Chen, Y.A., Chang, C.P., Yen, J.Y., Hooper, A., Yang, C.Y., 2011. Surface deformation from persistent scatterers SAR interferometry and fusion with leveling data: A case study over the Choushui River Alluvial Fan, Taiwan. Remote Sens. Environ. 115, 901–912. http://dx.doi.org/10.1016/j.rse.2010.11.007.

Jolivet, R., Agram, P.S., Lin, N.Y., Simons, M., Doin, M.P., Peltzer, G., Li, Z., 2014. Improving InSAR geodesy using global atmospheric models. J. Geophys. Res. Solid Earth 119, 2324–2341. http://dx.doi.org/10.1002/2013JB010588.

Jolivet, R., Grandin, R., Lasserre, C., Doin, M.P., Peltzer, G., 2011. Systematic InSAR tropospheric phase delay corrections from global meteorological reanalysis data. Geophys. Res. Lett. 38 (L17311), http://dx.doi.org/10.1029/2011GL048757.

Jung, J., Kim, D., Palanisamy Vadivel, S.K., Yun, S.H., 2019. Long-term deflection monitoring for bridges using X- and C-band time-series SAR interferometry. Remote. Sens. 11 (11), 1258. http://dx.doi.org/10.3390/rs11111258.

Liu, Q., Zhang, Y., Wei, J., Wu, H., Deng, M., 2021. HLSTM: Heterogeneous long short-term memory network for large-scale InSAR ground subsidence prediction. IEEE J. Sel. Top. Appl. Earth Obs. Remote. Sens. 14, 8244–8257. http://dx.doi.org/10.1109/JSTARS.2021.3106666.

Mirzaee, S., Amelung, F., Fattahi, H., 2023. Non-linear phase linking using joined distributed and persistent scatterers. Comput. Geosci. 178, 105291. http://dx.doi.org/10.1016/j.cageo.2022.105291.

Morgenstern, N.R., 1989. Recent experience with dam foundations on clay-shale in western Canada. In: Proceedings of the 12th International Conference on Soil Mechanics and Foundation Engineering. In: Special Lecture, vol. 4, pp. 2201–2208.

Nava, L., Carraro, E., Reyes-Carmona, C., Puliero, S., Bhuyan, K., Rosi, A., Monserrat, O., Floris, M., Meena, S.R., Galve, J.P., Catani, F., 2023. Landslide displacement forecasting using deep learning and monitoring data across selected sites. Landslides 20, 1263–1281. http://dx.doi.org/10.1007/s10346-023-02104-9.

Othman, A.A., Al-Maamar, A.F., Al-Manmi, D.A.M., Liesenberg, V., Hasan, S.E., Al-Saady, Y.I., Shihab, A.T., Khwedim, K., 2019. Application of DInSAR-PSI technology for deformation monitoring of the Mosul dam, Iraq. Remote. Sens. 11 (2632), http://dx.doi.org/10.3390/rs11222632.

Pedregosa, F., Varoquaux, G., Gramfort, A., Michel, V., Thirion, B., Grisel, O., Blondel, M., Prettenhofer, P., Weiss, R., Dubourg, V., Vanderplas, J., Passos, A., Cournapeau, D., Brucher, M., Perrot, M., Duchesnay, É., 2011. Scikit-learn: Machine learning in python. J. Mach. Learn. Res. 12, 2825–2830.

Peixeiro, M., 2022. Time Series Forecasting in Python. Simon and Schuster, New York.

Peng, M., Motagh, M., Lu, Z., Xia, Z., Guo, Z., Zhao, C., Liu, Q., 2024. Characterization and prediction of InSAR-derived ground motion with ICA-assisted LSTM model. Remote Sens. Environ. 301, 113923. http://dx.doi.org/10.1016/j.rse.2023.113923.

Pinyol, N.M., Alonso, E.E., Olivella, S., 2008. Rapid drawdown in slopes and embankments. Water Resour. Res. 44, W00D03. http://dx.doi.org/10.1029/2007WR006525.

Rosen, P.A., Gurrola, E.M., Agram, P., Cohen, J., Lavalle, M., Riel, B.V., Fattahi, H., Aivazis, M.A.G., Simons, M., Buckley, S.M., 2018. The InSAR scientific computing environment 3.0: A flexible framework for NISAR operational and user-led science processing. In: Proc. Int. Geosci. Remote Sens. Symp.. IGARSS, pp. 1119–1122. http://dx.doi.org/10.1109/IGARSS.2018.8517504.

Scholz, F.W., Stephens, M.A., 1987. K-sample Anderson–darling tests. J. Amer. Statist. Assoc. 82, 918–924. http://dx.doi.org/10.1080/01621459.1987.10478517.

Sharifi, S., Hendry, M., 2023. An improved estimation of surficial velocities obtained by MT-TOPSAR interferometry: A case study of Oldman River Dam, Alberta, Canada. Bull. Eng. Geol. Env. 82, 446. http://dx.doi.org/10.1007/s10064-023-03473-0.

Sutskever, I., Vinyals, O., Le, Q.V., 2014. Sequence to sequence learning with neural networks. arXiv preprint arXiv:1409.3215. https://arxiv.org/abs/1409.3215.

Tavakkoliestahbanati, A., Milillo, P., Kuai, H., Giardina, G., 2024. Pre-collapse space-borne deformation monitoring of the Kakhovka dam, Ukraine, from 2017 to 2023. Commun. Earth Env. 5, 145. http://dx.doi.org/10.1038/s43247-024-01284-z.

Truong, C., Oudre, L., Vayatis, N., 2020. Selective review of offline change point detection methods. Signal Process. 167, 107299. http://dx.doi.org/10.1016/j.sigpro.2019.107299.

Vaswani, A., Shazeer, N., Parmar, N., Uszkoreit, J., Jones, L., Gomez, A.N., Kaiser, Ł., Polosukhin, I., 2017. Attention is all you need. In: Advances in Neural Information Processing Systems. pp. 5998–6008. http://dx.doi.org/10.48550/arXiv.1706.03762.

Veličković, P., Casanova, A., Liò, P., Cucurull, G., Romero, A., Bengio, Y., 2018. Graph attention networks. In: 6th International Conference on Learning Representations, ICLR 2018 – Conference Track Proceedings. http://dx.doi.org/10.1007/978-3-031-01587-8_7.

Wright, T.J., Parsons, B.E., Lu, Z., 2004. Toward mapping surface deformation in three dimensions using InSAR. Geophys. Res. Lett. 31 (L01607), http://dx.doi.org/10.1029/2003GL018827.

Xiao, R., Jiang, M., Li, Z., He, X., 2022. New insights into the 2020 Sardoba dam failure in Uzbekistan from Earth observation. Int. J. Appl. Earth Obs. Geoinf. 107, 102705. http://dx.doi.org/10.1016/j.jag.2022.102705.

Xiao, Y., Tao, Q., Hu, L., Liu, R., Li, X., 2024. A deep learning-based combination method of spatio-temporal prediction for regional mining surface subsidence. Sci. Rep. 14, 19139. http://dx.doi.org/10.1038/s41598-024-70115-0.

Xie, L., Xu, W., Aoki, Y., 2025. Extracting a decadal deformation on Xiaolangdi upstream dam slope using seasonally inundated distributed scatterers InSAR (SIDS – InSAR). Int. J. Appl. Earth Obs. Geoinf. 138, 104462. http://dx.doi.org/10.1016/j.jag.2025.104462.

Xie, L., Xu, W., Ding, X., 2022a. Precursory motion and deformation mechanism of the 2018 Xe Pian-Xe Namnoy dam Collapse, Laos: Insights from satellite radar interferometry. Int. J. Appl. Earth Obs. Geoinf. 109, 102797. http://dx.doi.org/10.1016/j.jag.2022.102797.

Xie, L., Xu, W., Ding, X., Bürgmann, R., Giri, S., Liu, X., 2022b. A multi-platform, open-source, and quantitative remote sensing framework for dam-related hazard investigation: Insights into the 2020 Sardoba dam collapse. Int. J. Appl. Earth Obs. Geoinf. 111, 102849. http://dx.doi.org/10.1016/j.jag.2022.102849.

Yan, Y., Yu, H., Wang, Y., 2024. Alarming a tailings dam failure with a joint analysis of InSAR-derived surface deformation and SAR-derived moisture content. Remote Sens. Environ. 300, 113910. http://dx.doi.org/10.1016/j.rse.2023.113910.

Yunjun, Z., Fattahi, H., Amelung, F., 2019. Small baseline InSAR time series analysis: Unwrapping error correction and noise reduction. Comput. Geosci. 133, 104331. http://dx.doi.org/10.1016/j.cageo.2019.104331.

Zhang, L., Peng, M., Chang, D., Xu, Y., 2016. Dam Failure Mechanisms and Risk Assessment. John Wiley & Sons, Chichester, http://dx.doi.org/10.1002/9781118558522.

Zhou, C., Cao, Y., Gan, L., Wang, Y., Motagh, M., Roessner, S., Hu, X., Yin, K., 2024. A novel framework for landslide displacement prediction using MT-InSAR and machine learning techniques. Eng. Geol. 334, 107497. http://dx.doi.org/10.1016/j.enggeo.2024.107497.

Zhou, C., Ye, M., Xia, Z., Wang, W., Luo, C., Muller, J.-P., 2025. An interpretable attention-based deep learning method for landslide prediction based on multi-temporal InSAR time series: A case study of Xinpu landslide in the TGRA. Remote Sens. Environ. 318, 114580. http://dx.doi.org/10.1016/j.rse.2024.114580.